RSC Advances

PAPER

View Article Online
View Journal | View Issue



Cite this: *RSC Adv.*, 2026, **16**, 13915

# Development of multifunctional magnetic core–shell manganese $TiO_2$ photocatalysts for sustainable wastewater treatment: synergistic dye mineralization, antibacterial activity, and molecular docking insights

Sabahat Sabeen Butt,†[a] Shabnam Javaid,†[a] Muhammad Saqib Khan,*[ab] Rizwana Sarwar,[c] Sobia Ahsan Halim,[d] Muhammad Bilal,[a] Ajmal Khan,[de] Khayala Mammadova,[f] S. Tasqeeruddin,[g] Ahmed Al-Harrasi *[d] and Nadia Riaz *[a]

Photocatalytic oxidation using titanium dioxide ($TiO_2$) is a well-established and sustainable technology for addressing various water treatment challenges, particularly the persistent issue of textile wastewater. This study explores the synthesis and optimization of manganese-incorporated magnetic $Fe_3O_4/TiO_2$ (FeMnT) photocatalysts with enhanced photodegradation performance under visible light irradiation. The FeMnT photocatalysts were synthesized using a two-step process involving sol–gel assisted wet impregnation followed by calcination at temperatures ranging from 300 °C to 500 °C, exhibiting improved absorption in visible light, effective charge separation, and excellent photocatalytic breakdown of RY145 dye, along with easy magnetic recovery. The optimized photocatalyst, 0.75 FeMnT-300, demonstrated the highest degrading efficiency of all the produced nanocomposites, achieving 89.5% in just 60 minutes. Its enhanced structural properties, ideal photocatalyst dosage (1 g $L^{-1}$), and superior adsorption–desorption equilibrium at pH 6 contribute to its high efficiency. Because of the improved light penetration and more active catalytic sites, the dye removal efficiency was also noticeably greater at lower dye concentrations (*e.g.*, 10 mg $L^{-1}$). At the calcination temperatures for both 0.75 FeMnT-3 and 0.75FeMnT-5, 100% log reduction for *S. aureus* and *E. coli* was observed under visible light with an optimal dosage of 1 mg $mL^{-1}$ as the minimum bactericidal concentration (MBC), signifying efficient bacterial control. $Fe_3O_4$'s magnetic properties enabled rapid nanoparticle recovery, ensuring reusability and cost-effectiveness. The molecular docking studies revealed that the photocatalyst binds strongly to the active site of β-lactamase through multiple hydrogen, ionic, and metallic interactions with key catalytic residues, displaying a highly promising binding energy (−12.70 kcal $mol^{-1}$) that supports its strong bactericidal activity. Photoluminescence analysis indicated effective charge separation due to reduced emission intensity, while VSM measurements confirmed soft ferromagnetic behavior and adequate magnetization for recovery. These factors enhanced the photocatalytic performance of the optimized 0.75 FeMnT-3 photocatalysts. The strong relationship between dye discoloration and mineralization shows effective photocatalytic degradation, implying complete oxidative breakdown to give $^{\bullet}OH$ as the main ROS species rather than partial fragmentation of the dye molecule. These findings highlight the potential of FeMnT nanocomposites for efficient and sustainable wastewater treatment applications.

Received 25th January 2026
Accepted 4th March 2026

DOI: 10.1039/d6ra00672h

rsc.li/rsc-advances

[a]*Department of Environmental Sciences, COMSATS University Islamabad, Abbottabad Campus, 22060, Pakistan. E-mail: nadiariazz@gmail.com*

[b]*Department of Environmental Science, Institute of Environmental Sciences and Engineering, School of Civil and Environmental Engineering, National University of Science and Technology, 44000, Islamabad, Pakistan. E-mail: muhammadsaqib@yahoo.com*

[c]*Department of Chemistry, COMSATS University Islamabad, Abbottabad Campus, 22060, Pakistan*

[d]*Natural and Medical Sciences Research Center, University of Nizwa, P.O. Box 33, Birkat Al Mauz, Nizwa 616, Sultanate of Oman, Oman. E-mail: aharrasi@unizwa.edu.om*

[e]*Department of Chemical and Biological Engineering, College of Engineering, Korea University, Seoul 02841, Republic of Korea*

[f]*Medical and Biological Physics Department, Azerbaijan Medical University, Baku, Azerbaijan*

[g]*Department of Pharmaceutical Chemistry, College of Pharmacy, King Khalid University, Abha 62529, Saudi Arabia*

† These authors contributed equally to this work.

# 1 Introduction

Water pollution, particularly from industrial organic pollutants, remains one of the most pressing environmental challenges today. Among the various industries contributing to this problem, the textile sector plays a significant role, discharging large quantities of dye-containing effluents into water bodies. These dyes, particularly azo and reactive dyes, pose a serious threat to aquatic ecosystems. Azo dyes, commonly used in textiles, are responsible for severe contamination due to their persistence, toxicity, and ability to interfere with light penetration in water, which in turn disrupts the oxygen balance required for aquatic life.[1,2] Reactive Yellow 145 (RY145), a commonly used reactive dye, is of particular concern due to its solubility in water, which makes it challenging to remove using conventional wastewater treatment methods such as activated carbon adsorption, coagulation, or membrane filtration.[3]

The disposal of dye-laden wastewater into the environment can lead to numerous health issues, including allergic reactions, dermatitis, and even carcinogenic effects in humans.[4] It is estimated that more than $7 \times 10^7$ tons of dyes are produced annually, with a significant portion of azo dyes 15–50%, ending up in wastewater streams, further exacerbating water pollution.[5] In addition to their toxicity, these dyes also reduce light penetration and deplete dissolved oxygen levels in water bodies, creating an inhospitable environment for aquatic organisms.[6] This underscores the urgent need for effective methods to treat textile effluent and remove dyes from contaminated water.

Traditional wastewater treatment and disinfection technologies, including physical, biological, and chemical methods, are often ineffective against dye pollutants due to their complex chemical structures and synthetic nature[7] and generation of disinfection byproducts. Consequently, there has been increasing interest in advanced oxidation processes (AOPs) as a more effective solution for dye degradation. Among these, photocatalytic degradation using semiconductor materials such as $TiO_2$ has emerged as a promising method due to its ability to degrade a wide range of organic pollutants under UV light irradiation.[8] However, the main limitations of $TiO_2$-based photocatalysis include the high energy requirements for UV activation and the difficulty of separating the photocatalyst from treated effluents. Moreover, $TiO_2$'s small size may cause filter clogging, and replacement or regeneration may decrease the disinfection process's effectiveness and overall cost.

Core–shell magnetic nanocomposites, specifically $Fe_3O_4/TiO_2$, have gained recognition as effective photocatalysts for the degradation of textile dyes due to their easy magnetic separation, excellent stability, and photocatalytic performance. Although magnetite nanoparticles ($Fe_3O_4$) are non-toxic, affordable, and can be easily retrieved with a magnet, their inherent photocatalytic properties are somewhat limited. This limitation requires the addition of semiconductor shells like $TiO_2$ to facilitate advanced oxidation processes (AOPs) through the creation of reactive oxygen species (ROS) under UV/visible light. Recent developments have improved these systems by introducing transition metals such as manganese (Mn) into the $TiO_2$ shell, resulting in $Fe_3O_4$@Mn–$TiO_2$ tri-composites. The incorporation of Mn not only alters the electronic structure of $TiO_2$, enabling it to absorb visible light, but also improves charge separation and reactive species production, leading to greater degradation efficiencies for azo dyes like Reactive Yellow 145. In this study, $Fe_3O_4/TiO_2$@Mn nanocomposites were synthesized using a sol–gel method, allowing for controlled deposition of Mn-modified $TiO_2$ on $Fe_3O_4$ cores, producing magnetically recoverable photocatalysts with optimized mass ratios. The presence of $Fe_3O_4$ ensures a consistent magnetic response, making separation easy with a super magnet, while Mn doping enhances photocatalytic effectiveness under UV-vis light. Kinetic studies for the degradation of model dyes were conducted using the Langmuir–Hinshelwood model, demonstrating that Mn-modified $Fe_3O_4/TiO_2$ offers improved photodegradation efficiency along with easy recyclability, providing a cost-effective and eco-friendly approach for treating textile wastewater.

To overcome these challenges, several strategies have been developed to enhance the photocatalytic performance of $TiO_2$ and make it more practical for large-scale applications. One such approach involves doping $TiO_2$ with metal or non-metal elements to reduce its band gap, enabling it to absorb visible light more efficiently.[9] Metal doping, such as incorporating manganese (Mn) into TiO,[2] has been shown to improve its photocatalytic activity under visible light.[10] Furthermore, the development of core–shell nanostructures, where $TiO_2$ serves as the shell and a magnetic core (such as $Fe_3O_4$) is embedded within, has provided a promising solution to the photocatalyst recovery problem.[11] These magnetic core–shell composites allow for easy separation of the photocatalyst from water using an external magnetic field, making the process more cost-effective and environmentally friendly.[12] The objective of this study is to develop a magnetic core–shell composite consisting of $Fe_3O_4$ nanoparticles as the core and $TiO_2$ as the shell for the photocatalytic degradation of RY145 dye under visible light. This approach aims to combine the high photocatalytic degradation and disinfection efficiency of $TiO_2$ with the magnetic recovery capability of $Fe_3O_4$, thereby enhancing both the efficiency and sustainability of the treatment process. Molecular docking was conducted to examine the binding mechanism of bactericidal activity. The photocatalyst's strong contact with the active site of β-lactamase may limit enzyme function, leading to antibacterial efficacy against β-lactam-resistant bacteria. By optimizing the synthesis of this composite, we aim to provide a cost-effective and reusable solution for disinfection and treatment of textile dye-contaminated wastewater.

# 2 Materials and methods

The reagents used during synthesis and reaction study are reported in Table S1. The commercial RY145 double azo dye, obtained from Koh-e-Nor textile mills, Rawalpindi Pakistan. All the chemicals were used as received, without purification.

### 2.1. Synthesis of nanoparticles, bi-composites and tri-composites

A range of nanoparticles, including $Fe_3O_4$ and $TiO_2$, as well as bicomposites ($Fe_3O_4/TiO_2$) and magnetic manganese-doped

 

titania tri-composites, were synthesized using previously described methodologies. A two-step synthesis technique was used to synthesize magnetic core–shell nanocomposites of Mn@$Fe_3O_4$/$TiO_2$. In the first step, $Fe_3O_4$/$TiO_2$ was synthesized utilizing a modified sol–gel approach followed by the addition of manganese to the magnetic titania in the second phase using the wet impregnation (WI) method.

The $Fe_3O_4$ magnetic nanoparticles (Fe-NP) were prepared using a chemical precipitation approach, mixing $FeSO_4 \cdot 7H_2O$ and $FeCl_3 \cdot 6H_2O$ solutions, reducing the pH to 10 with $NH_4OH$, filtering the black precipitate, followed by washing and drying the resulting nanoparticles as described in.[13] $TiO_2$ nanoparticles were synthesized employing sol–gel method[14] by dropwise rigorously mixing solution A (37 mL of TTIP, 60 mL of ethanol, and 15 mL of acetic acid) with solution B (14 mL of ethanol, 10 mL of acetic acid, and distilled water) till gel formation, followed by aging (24 hours), drying (100 °C for 24 hours), grinding to a fine powder and annealing at different calcination temperatures (300–500 °C). A single-step-modified sol–gel method was used to synthesize $Fe_3O_4$/$TiO_2$ as reported above, except for the addition $Fe_3O_4$ (required amount) in isopropyl alcohol (solution B) after ultrasonicating for 30 minutes to ensure dispersion. Manganese-doped magnetic titania tri-composites were synthesized using a modified two-step method, where, Manganese sulfate monohydrate ($MnSO_4 \cdot H_2O$) as manganese precursor salt was doped onto already synthesized $Fe_3O_4$/$TiO_2$ bicomposites *via* wet impregnation, followed by drying at 105 °C for 24 hours and annealing at 300, 400, and 500 °C for 1 hour. The final activated photocatalyst was stored in a desiccator. The synthesized composites were given codes for clear understanding as follow: *x*-FeMnT-*y*, where *x* represents the amount of $Fe_3O_4$ with varying loadings and *y* refers to the calcination temperature (300–500 °C).

### 2.2. Photocatalytic degradation/disinfection study

Photodegradation studies were carried out to assess the degradation efficiency of synthesized photocatalysts. A typical photodegradation test involved ultrasonically dispersing 1 mg $mL^{-1}$ of nanoparticles in distilled water to guarantee a homogeneous suspension and then adding the model dye solution to get the specified concentration. Before being subjected to light irradiation from above (using a photoreactor equipped with a 500 W halogen lamp), the reaction solution had been stirred in dark conditions for 30 minutes to achieve an adsorption–desorption equilibrium. Reaction samples were taken at specific times (10, 20, 30, 40, 50, and 60 min) during the irradiation process. The same procedures were used for adsorption experiments, but no light exposure was applied. The reaction samples were centrifuged, the photocatalysts were separated using an external magnetic field, and samples were analyzed using a UV-vis spectrophotometer (PG Instruments T80+ series) to track changes in dye concentration. Control experiments were also conducted without light or nanomaterials for comparison. The absorbance spectrum of the reaction solution was monitored between 200 and 800 nm, and a typical RY145 peak at 420 nm was used for quantification. An established calibration curve was made using known RY145 concentrations. Using eqn 1, the percentage of dye discoloration was calculated to determine the change in dye concentration over time.

$$\text{Dye discoloration}(\%) = \left(\frac{C_0 - C_f}{C_0}\right) \times 100 \quad (1)$$

where: $C_0$ is initial dye concentration (mg $L^{-1}$) and $C_f$ is the dye concentration (mg $L^{-1}$) at different interval of time for the period of light irradiation.

$$\text{Dye mineralization}(\%) = \left(\frac{C_0 - C_f}{C_0}\right) \times 100 \quad (2)$$

where: $C_0$ is initial COD (mg $L^{-1}$) and $C_f$ is the COD (mg $L^{-1}$) at different interval of time.

In optimization studies on RY145 decolorization under various reaction conditions, such as photocatalyst dose (0.1 to 2 mg $mL^{-1}$), pH (2 to 12), and initial dye concentration (10 to 200 g $L^{-1}$), the most effective photocatalyst was used.

Antibacterial evaluation of synthesized FeMnT nanomaterials was conducted in two phases: initial screening of synthesis parameters followed by performance optimization based on reaction conditions (type of bacterial pathogens, irradiation time or kill time analysis (KTA), and minimum bactericidal concentration (MBC)), focusing on the nanomaterial exhibiting maximum bacterial inhibition. To ensure sterility, all culture media, broth, and glassware were autoclaved prior to experimentation. Antibacterial effectiveness was evaluated using the plate count method performed by placing the photoreactor (using a photoreactor equipped with a 500 W halogen lamp) inside a laminar flow hood while ensuring sterile conditions. The nanomaterial (1 mg $mL^{-1}$) was added to a bacterial suspension ($10^4$ CFU per mL), and samples were collected at specific intervals during irradiation, plated on agar, incubated (at 37 °C for 24 hours in an incubator), and analyzed for viable colonies using a colony counter. Control experiments were conducted without light (in the dark, by keeping all experimental conditions the same except for light and with nanomaterial for comparison. Results were reported as a % log reduction before and after the photocatalytic oxidation (PCO) using the following formula. The percent log reduction formula is used to quantify the reduction in the number of bacteria after a treatment or process. It is calculated based on the initial count of microorganisms before treatment and the count after treatment. The "log reduction" refers to the logarithmic reduction in the number of microorganisms. To calculate log reduction, the logarithm of the ratio of the initial count to the count after treatment is used. The formula for log reduction is:

$$\%\ \text{log reduction} = \frac{(A_0 - A_t)}{A_0} \times 100 \quad (3)$$

where $A_0$ indicates the log of the number of viable bacteria before PCO and $A_t$ denotes the log of the number of viable bacteria after PCO.

### 2.3. Kinetic and mechanistic investigation of photocatalytic degradation of RY145

Pollutant adsorption on nanomaterials has a major impact on photocatalysis, a surface phenomenon that involves chemical

reactions on solid surfaces. Pollutant photodegradation has unique kinetics that vary depending on whether the process is discoloration or mineralization. For effective quantitative analysis, experimental dye photodegradation data must be fitted to the Langmuir–Hinshelwood (LH) model.[15] The LH model was used to examine the relationship between the photodegradation rates and treatment time for Mn@$Fe_3O_4$/$TiO_2$ photocatalysts under visible light exposure.

$$r_0 = \frac{\mathrm{dRYDye}}{\mathrm{d}t} = \frac{k_c K_{ads} \mathrm{Dye}}{1 + K_{ads} \mathrm{Dye}} \quad (4)$$

where d$t$ is the change in reaction time, $k_c$ is the rate constant, $K_{ads}$ is the adsorption coefficient, and dye is the change in model dye concentration.

Experiments with selective scavengers were carried out to determine the active species involved. To adjust ionic strength, the following scavengers were used: $AgNO_3$ (1 mM) as an electron scavenger, $CaCl_2$ (1 mM) as a hole ($h^+$) scavenger, benzoquinone (BQ, 1 mM) for superoxide radicals ($O_2^{\bullet -}$), and isopropanol (IPA, 1 mM) for $^{\bullet}$OH radicals. Before irradiation, each scavenger was added to the reaction mixture, and spectrophotometric monitoring was used to track the RY145 degradation.

### 2.4. Characterization of the photocatalyst

Thermogravimetric analysis (TGA) was conducted to assess the thermal stability and compositional variations of the synthesized raw FeMnT nanomaterials. Powder X-ray diffraction (XRD) was used to evaluate the crystalline structure and phase composition of the produced samples using Cu K$\alpha$ radiation ($\lambda$ = 1.5406 Å) throughout a suitable 2$\theta$ range. SEM was used to analyze the morphology of FeMnT-3. Energy-dispersive X-ray spectroscopy (EDS) was used in conjunction with the SEM system to confirm the element content and distribution. To assess the recombination behavior of photogenerated electron–hole pairs, PL spectra were obtained at room temperature using an excitation wavelength of 325 nm. The magnetic characteristics of $Fe_3O_4$-containing nanocomposites were evaluated at room temperature using a vibrating sample magnetometer (VSM) to estimate saturation magnetization ($M_s$), remanence ($M_r$), and coercivity ($H_c$), verifying their magnetic recoverability. Surface functional groups were identified using Fourier-transform infrared spectroscopy (FTIR), and metal–oxygen bonding interactions were confirmed.

### 2.5. Molecular docking

Molecular docking was conducted to examine the binding mechanism of the bactericidal activity of $Fe_3O_4$/$TiO_2$ using Molecular Operating Environment (MOE version 2024.06). A three-dimensional structure of *E. coli* β-lactamase (PDB ID: 1ERM, (68) resolution = 1.70 Å) in complex with boronic acid inhibitor (1*R*)-1-acetamido-2-(3-carboxyphenyl)ethane boronic acid was taken from Protein Databank. The enzyme was prepared for docking by adding hydrogen atoms and partial charges (according to the AMBER12:EHT force field). Only water molecules within the 3 Å vicinity of the active site were retained, while the rest were removed. The structure of ligand was generated on MOE with OPLS-AA force field with the given parameters for Fe (mass = 55.8500, $q = -2.00$, $R = 1.200$, $E_{ps}$ = 0.0500, $m = 12$, and $n = 6$), and Ti (mass = 47.8670, $q = -2.00$, $R$ = 1.5875, $E_{ps} = 0.1304$, $m = 12$, and $n = 6$). The default docking method of MOE was initially tested by re-docking of the co-crystallized boronic acid inhibitor with the default settings (*e.g.*, triangle matcher algorithm and London dG scoring function) with 50 docked and 30 refined solutions. The re-docking results showed appropriate results with a docking score of −7.89 kcal mol$^{-1}$ and RMSD of 2.23 Å. Thus, the same docking protocol was applied to dock our ligand with 50 poses and 30 refined poses with the GBVI/WSA dG function. The best docked conformation was chosen based on the docking score and binding interactions.

## 3 Results and discussion

### 3.1. Photocatalytic degradation of RY145: screening

Screening studies were carried out to determine the photocatalysts with the highest efficiency for RY145 photodegradation. A series of photocatalysts were developed (with varied $Fe_3O_4$ loading (0–1.5 wt%) and calcination temperature (300 and 500 °C) and were assessed for RY145 photodegradation. Following screening against the photocatalyst's dosage, initial RY145 concentration, and irradiation period, the best photocatalyst was chosen to perform additional reaction optimization. The efficiency of the Mn salt, bare nanomaterials such as $Fe_3O_4$, bare $TiO_2$, and metal oxide doped photocatalysts $Fe_3O_4$/$TiO_2$ (FeT) and as well as the optimum photocatalyst 0.75 FeMnT-3 under visible light irradiation, was further assessed using multiple blank tests. Fig. 1(a) illustrates how the material's performance was enhanced by 89.5% RY145 photodegradation after 60 minutes of irradiation when a photocatalyst and light were introduced. A modest decrease in RY145 concentration (1.69%), however, was seen in the DL reaction studies, indicating photolysis (where DL refers to simply exposing dye solution under light without photocatalyst). Furthermore, when exposed to light, 0.75FeT-3 eliminated 62.87% whereas, variable removal efficiency for Mn salt (20.2%), $TiO_2$ (62.45%) and $Fe_3O_4$ (65.82%) were observed. The analysis highlights the improved efficiency of $Fe_3O_4$/$TiO_2$-based photocatalysts, as well as the need to adjust photocatalyst composition and conditions for efficient photodegradation.

The photocatalytic process's efficacy is strongly influenced by the annealing temperature and duration. FeMnT photocatalysts were calcined at temperatures of 300 °C and 500 °C with $Fe_3O_4$ loadings varying from 0.1 to 1 weight percent (wt%), and their photocatalytic activity was monitored for 60 minutes. Fig. 1(b) shows how calcination temperature and $Fe_3O_4$ loading affect photocatalyst performance. The optimum combination was 0.75 wt% $Fe_3O_4$ loading calcined at 300 °C, which achieved the maximum RY145 removal efficiency of 89.5% within 60 minutes of visible light irradiation. Lower calcination temperatures (300 °C) performed better than higher temperatures (500 °C), which may be attributed to the reduction of active sites due to the structural changes of the catalysts caused by high-

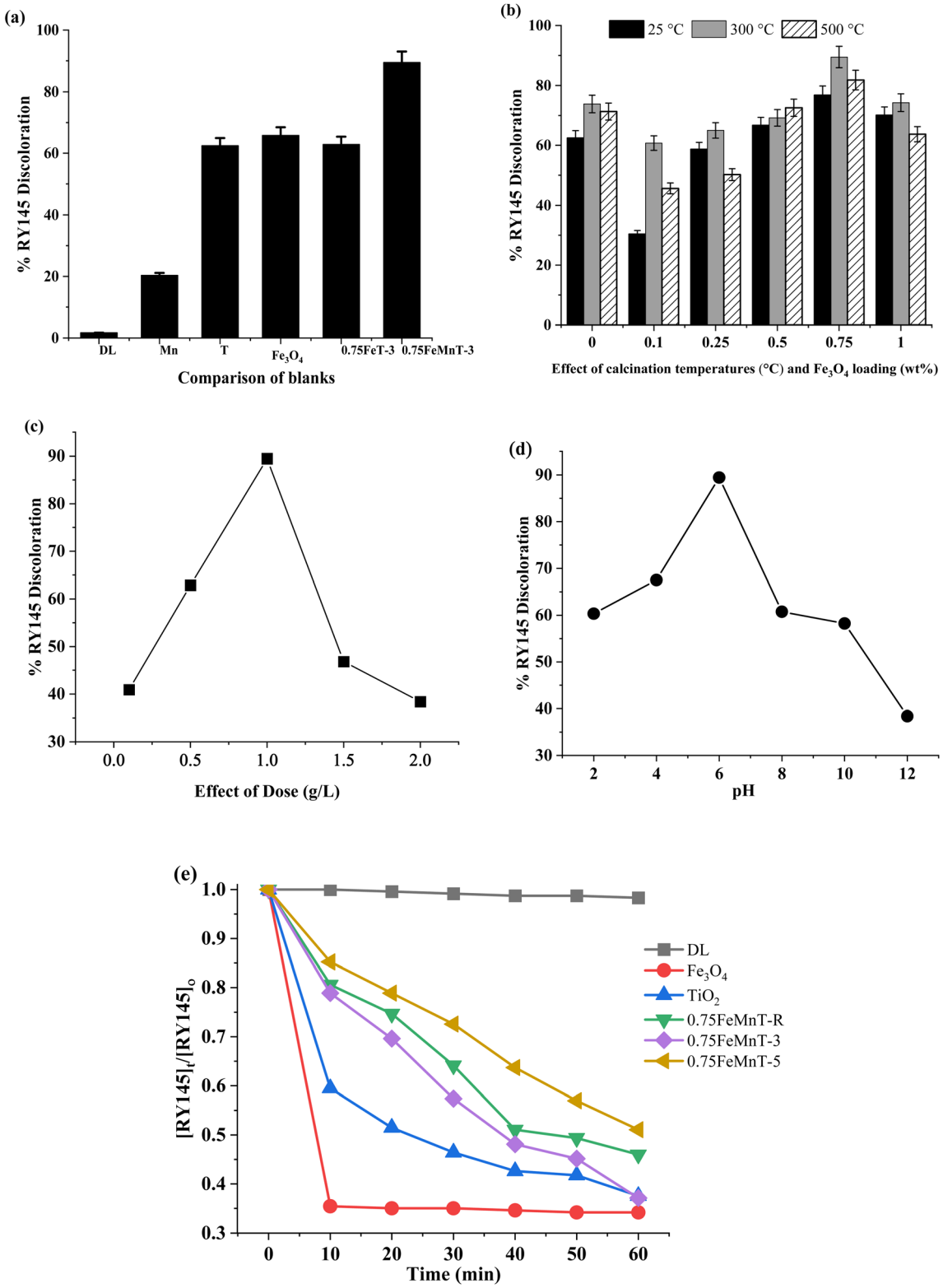


Fig. 1 (a) Comparison of degradation efficiency of blanks and 0.75 FeMnT (b) effect of metal loading and calcination temperature (c) effect of photocatalyst dose (d) effect of pH (e) effect of irradiation time on % RY145 discoloration using 0.75 FeMnT calcined at NC (un-calcined), 300 °C and 500 °C. T = Bare $TiO_2$ calcined at 300 °C; 0.75 FeMnT = Mn@$Fe_3O_4$/$TiO_2$ calcined at 300 °C and 500 °C; irradiation time = 60 minutes; DL = Dye solution under light without photocatalyst.

temperature calcination,[16] reducing 0.75 FeMnT-3 photocatalytic performance.

### 3.2. Photocatalytic performance optimization

**3.2.1. Effect of photocatalyst dose.** Fig. 1(c) shows that increasing the photocatalyst dose of 0.75 FeMnT-3 from 0.1 to 2 g $L^{-1}$ improved the dye removal efficiency of RY145, which increased from 40.93% to nearly 89.5%. The optimized dose for maximal RY145 removal was found to be 1 g $L^{-1}$. However, as the dose increased to 2g $L^{-1}$, the removal efficiency dropped drastically (89.40% to 38.40%). This decrease in efficiency at higher doses is most likely due to a large number of photocatalyst particles, which cause light scattering and shielding effects.[17] The aforementioned phenomena limit the penetration of light into the reaction media and the activation of photocatalytic sites, slowing the overall photocatalytic process. This finding emphasizes the need of adjusting photocatalyst amount to maintain active site accessibility and light-absorbing efficacy to achieve effective dye degradation.

**3.2.2. Effect of initial pH.** Reaction pH plays a pivotal role in the photocatalytic degradation of dyes, with slightly acidic conditions proving to be the most effective for RY145 removal. Fig. 1(d) illustrates the degradation behavior of RY145 dye under varying pH levels. In acidic conditions (pH 2–6), the discoloration of the dye improved from 60.33% to 89.5%, demonstrating enhanced photocatalytic activity within this range. Conversely, in alkaline conditions (pH 8–12), the removal efficiency decreased from 60.76% to 38.40%. This decline in performance at higher pH levels is likely attributed to a reduction in the photocatalyst's surface charge,[18] which hinders dye adsorption, and to alterations in the charge state of the RY145 dye. The maximum photodegradation efficiency, 89.5%, was attained with 0.75 FeMnT-3 at pH 6 (working pH), indicating that this pH was suitable for the process.

**3.2.3. Effect of irradiation time.** The photodegradation efficiency of RY145 under visible light irradiation was evaluated as a function of visible light exposure time using various synthesized photocatalysts. The results are depicted in Fig. 1(e). The control experiment, conducted using bare $TiO_2$ under visible light (designated as "T"), achieved a 70% removal efficiency. In contrast, the 0.75 FeMnT-3 photocatalyst demonstrated much better performance, achieving over 89% degradation of RY145 within the same time frame. This efficiency was observed both in the uncalcined form and after calcination at 300 °C and 500 °C. The enhanced photocatalytic activity of the 0.75 FeMnT-3 catalyst can be attributed to its optimized structural and optical properties, which are improved at an optimized (300 °C) calcination temperature. These characteristics are likely to enable more efficient light absorption and facilitate the effective degradation of RY145.

### 3.3. Kinetic study of photocatalytic degradation of RY145

The influence of initial dye concentration on photodegradation activity was investigated by keeping the 0.75 FeMnT-3 photocatalyst and other parameters constant while altering the dye concentration between 10 and 100 mg $L^{-1}$. The results of different order of reactions are depicted in Fig. 2 (a–d). The photodegradation efficiency of RY145 declines as the dye concentration increases, with the highest efficiency recorded at 10 mg $L^{-1}$ (98.63%), followed by 20 mg $L^{-1}$ (89.45%), 50 mg $L^{-1}$ (77.53%), 70 mg $L^{-1}$ (74.53%), and the lowest at 100 mg $L^{-1}$ (62.73%). The results reveal that raising the dye concentration above 50 mg $L^{-1}$ considerably reduces the photocatalytic efficacy. At dye concentrations below 50 mg $L^{-1}$, the maximum discoloration rates (89.5%) have been observed, while the lowest removal effectiveness (62.73%) was found at dye concentrations of 100 mg $L^{-1}$. These findings imply that higher dye concentrations reduce photocatalytic efficacy, most likely due to increased competition for active sites on the photocatalyst surface and less light penetration into solutions. As the dye concentration increases, the amount of accessible light for photocatalysis decreases, limiting the degradation process. As a result, the findings suggest that dye concentration is inversely proportional to the efficiency of RY145 removal. Fig. 2 shows the impact of model dye RY145 varying concentrations on photocatalytic efficacy. When the performance of 0.75 FeMnT-3 against varying RY145 concentrations was plotted as ln $[RY145]_0/[RY145]_t$ against irradiation duration (min), as shown in Fig. 2(c), a linear relationship was obtained. The $K_{app}$ (apparent first-order rate constant) is the same as the linear regression's slope. As a result, the 0.75 FeMnT-3 tri-composites' discoloration performance belongs to the pseudo-first-order reaction kinetics. The Langmuir–Hinshelwood (LH) model predicts (Fig. 2(e)), the rate of dye degradation ($r_0$) for different dye concentrations, with $k_c = 0.0323$ mg $L^{-1}$ $min^{-1}$ and $K_{ads}$ or $K_{LH} = 1.9928$ L $mg^{-1}$. These constants demonstrate that the reaction rate is proportional to both catalytic activity ($k_c$) and adsorption efficiency ($K_{ads}$). Higher $K_{ads}$ indicate an effective adsorption of dye molecules onto the catalyst surface, while $k_c$ regulates the intrinsic rate of photodegradation under optimal adsorption conditions.

### 3.4. Photocatalytic degradation/disinfection

The FeMnT photocatalysts were optimized for antibacterial efficacy against *S. aureus* (G+ive) and *E. coli* (G−ive) by assessing $Fe_3O_4$ as dopant concentration (0.1–5 mol%) and calcination temperatures (300 °C and 500 °C). From the results (Fig. 3(a)), it is evident that dopant concentration is a major factor influencing photocatalytic disinfection, with 0.75 mol% as an optimum concentration with 100% log reduction of *S. aureus* at lower calcination temperatures. It was observed that samples calcined at 300 °C outperformed those at 500 °C, indicating that lower-temperature calcination enhances bacterial inhibition, likely due to better phase stability and surface area of the photocatalysts.

Considering different pathogens (*E. coli* and *S. aureus*), Fig. 3(b) compares bacterial susceptibility, exposing *S. aureus* as more susceptible, exhibiting higher log reductions (100% at 0.75 FeMnT-3 and 84.95% at 0.75FeMnT-5) compared to *E. coli* (76.14% and 72.15%, respectively). This difference is ascribed to structural dissimilarities as G+ive and G−ive: *E. coli*'s outer membrane offers greater oxidative stress resistance. At the same

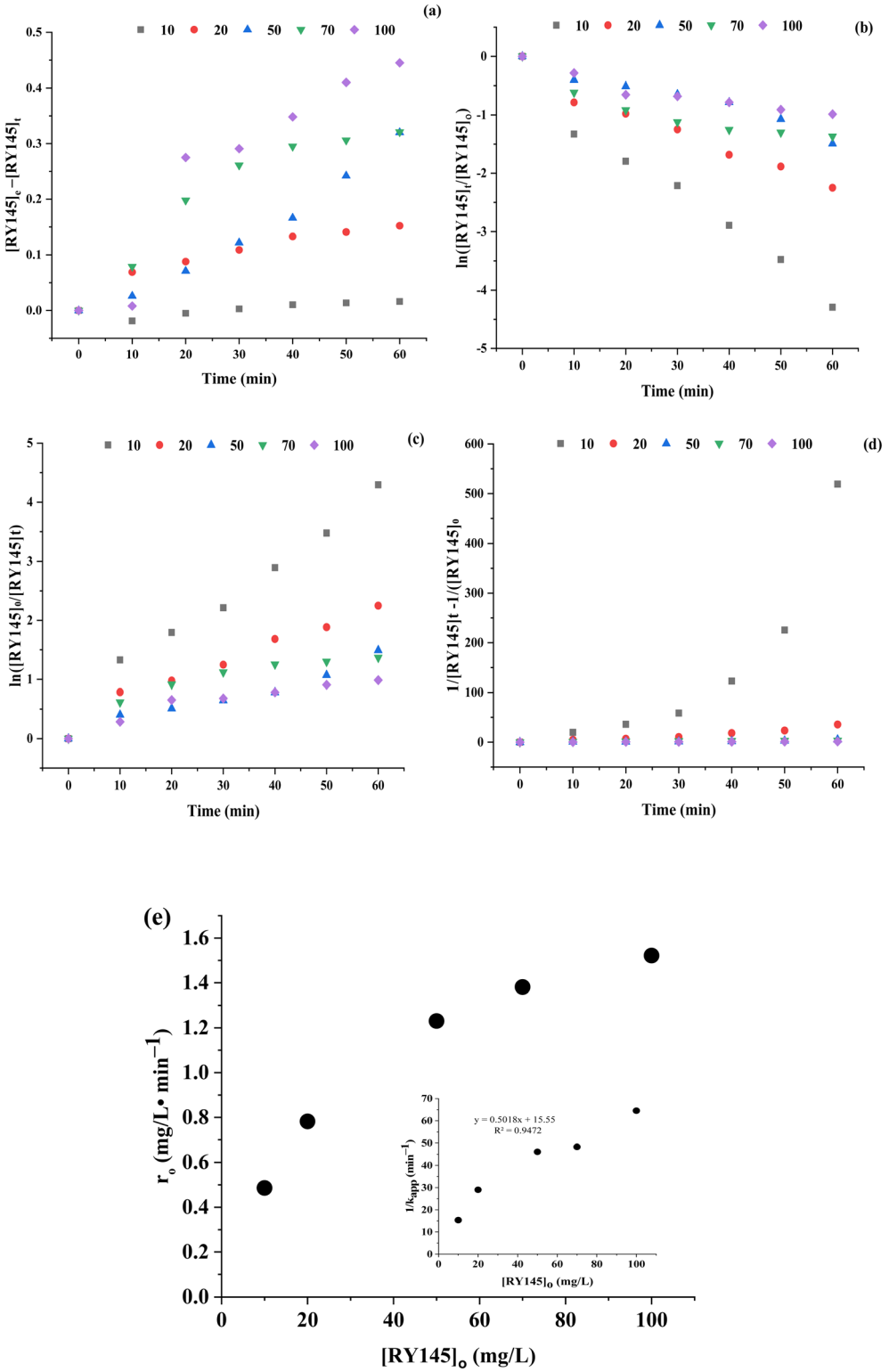


Fig. 2 Kinetic analysis of the photocatalytic degradation of reaction RY145 at different initial concentration (a) zero order kinetic model (b) first order kinetic model (c) Pseudo-first and (d) second order kinetic model (e) the influence of RY145 concentration on photodegradation rate using 0.75 FeMnT-3 (insert) Plot of the reciprocal of the pseudo-first order rate constant *vs.* RY145 concentrations.

time, *S. aureus*'s thicker peptidoglycan layer is less protective against reactive oxygen species (ROS). These findings align with prior studies show enhanced $TiO_2$-mediated photocatalytic activity with Mn and Ni dopants.[19,20]

To determine the optimal photocatalyst dosage as minimum bactericidal concentration (MBC), NC concentrations of 0.5, 1, and 1.5 mg $mL^{-1}$ were assessed (Fig. 3(c)). Results showed that *S. aureus* achieved a 100% log reduction at

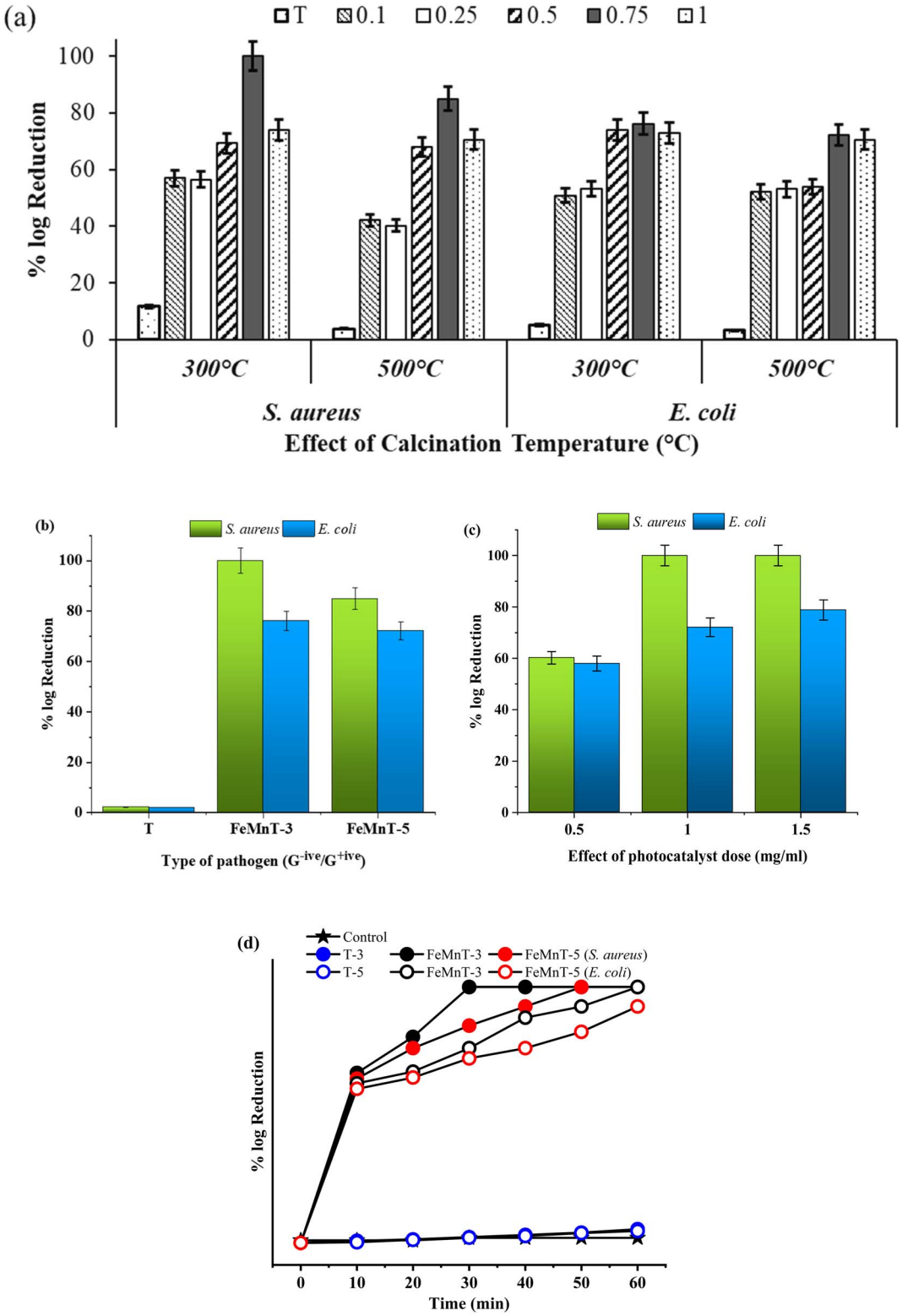


Fig. 3 Percent log reduction using FeMnT (a) dopant concentration (0.1–5 mol%) and calcination temperatures (300 °C and 500 °C) (b) different pathogens (*E. coli* and *S. aureus*) (c) determination of Minimum Bactericidal Concentration (MBC) (d) kill time analysis against *S. aureus* using control, Bare $TiO_2$ and 0.75FeMnT calcined at different calcination temperatures (300 °C and 500 °C) against *E. coli* and *S. aureus*.

1 mg $mL^{-1}$, whereas *E. coli* achieved only 72.15%, highlighting *S. aureus*'s superior susceptibility. Raising the quantity to 1.5 mg $mL^{-1}$ further improved inactivation but with diminishing returns, suggesting 1 mg $mL^{-1}$ as the optimal concentration for bacterial disinfection. Comparatively, $Fe_3O_4$-TNS at 100 μg $mL^{-1}$ achieved 87.2% (*E. coli*) and 93.7%

(*S. aureus*) inhibition after two hours of simulated solar irradiation in a previously reported study.[21]

Time-dependent bacterial inhibition, as illustrated in the kill time assay in Fig. 3(d), demonstrated a fair increase in % log reduction over 60 minutes. Notably, 0.75 FeMnT-3 and 0.75FeMnT-5 achieved 100% inhibition after 40 minutes, confirming their efficacy. The said 99% bacterial reduction at 60 minutes highlights the superior antibacterial properties of FeMnT photocatalysts. The role of Mn doping in $TiO_2$ is significant, as it improves visible-light absorption, suppresses electron–hole recombination, and increases surface adsorption, thereby improving bacterial inactivation efficiency.[22] These findings establish FeMnT as an effective photocatalyst for water disinfection, particularly under solar irradiation.

### 3.5. Characterization of the photocatalyst

The initial step in our process involved assessing the thermal stability of $TiO_2$ before using it as a shell for an iron core, a crucial step in creating a triplicate catalyst. It was essential to determine this stability due to the temperature increase during the calcination process.[23] Thermal Gravimetric Analysis (TGA) results in Fig. 4(a) illustrate the change in residual mass of the samples with an increase in temperature. The initial weight loss, which was less than 3.7% up to 100 °C, can be attributed to the presence of residual physically adsorbed water and solution solvents. Subsequently, a weight loss of approximately 15% was observed for nanoparticles generated through chemical precipitation within the temperature range of 200 °C to approximately 800 °C.

The FTIR analysis of titania and FeMnT-3 proved to be an effective method for evaluating the early physicochemical properties of nanoparticles, as illustrated in Fig. 4(b). The presence of manganese, iron, and titania was confirmed as the most abundant component, evidenced by the strong intensity of the bands observed at 970 $cm^{-1}$ and 1800 $cm^{-1}$. The product exhibited highly distinctive and sharp stretching bands associated with manganese iron titania, spanning the range of 751 $cm^{-1}$ to 1768 $cm^{-1}$.

The XRD analysis of raw titania, calcined titania (300 °C) identified characteristic peaks labeled at angles of 25, 38, 63, 67, and 76 as shown in Fig. 4(c). The FeMnT-3 showed the characteristic peaks labeled at an angle of 25, 34, 38, 48, 57, and 67 as shown in Fig. 4(c). The sample produced was confirmed to be manganese iron titania by XRD examination, with raw titania, calcined titania, and sample ($2\theta = 25°$, $2\theta = 67°$) being the most common polymorph formed in the raw titania, calcined titania, and manganese iron titania samples.

Photoluminescence (PL) spectroscopy was used to analyze the photogenerated electron–hole pairs' recombination behavior. In general, higher PL intensity in Fig. 4(d) suggests increased radiative recombination, whereas lower PL emission indicates superior charge separation and lower recombination rates. The optimized 0.75 FeMnT-3 sample shows a prominent emission band in the ~500–520 nm range with significantly lower intensity compared to bare $TiO_2$, showing excellent suppression of electron–hole recombination. This decreased PL response indicates that Fe/Mn inclusion and structural optimization efficiently modify defect states and enhance interfacial charge transfer, hence reducing radiative recombination pathways. The reduced PL intensity is directly related to 0.75 FeMnT-3's enhanced photocatalytic activity, which achieved 89.5% photodegradation in 60 minutes. According to similar studies reported by Palliyalil *et al.*,[24] the Fe–Mn–$TiO_2$ heterostructure (TFM system) exhibited several emission peaks in the visible region, which are attributed to surface defects, oxygen vacancies, and bulk trap states. While such defect states can improve visible light absorption, too high defect-induced trap levels can generate competing recombination centers, limiting effective charge separation. Compared to the ACSAMI system's defect-rich multi-peak emission profile, 0.75 FeMnT-3's significantly suppressed and simpler PL response suggests a better-regulated defect environment and improved carrier dynamics. Although both systems employ Fe/Mn modification strategies to enhance photocatalytic performance, the optimized 0.75 FeMnT-3's nanocomposite demonstrates more efficient recombination suppression. This is consistent with its enhanced photocatalytic efficiency under the current experimental conditions.

The magnetic response of the bare $Fe_3O_4$ and FeMnT-3 heterostructure was assessed using vibrational sample magnetometry (VSM). The magnetic hysteresis loops for both samples (Fig. 4(e) and (f)) display characteristic *S*-shaped curves, indicating soft magnetic characteristics. The $Fe_3O_4/TiO_2$ (Fig. 4(e)) had a saturation magnetization ($M_s$) of around 61–62 emu $g^{-1}$, indicating that the $Fe_3O_4$ phase maintained its high magnetic ordering. The Mn-modified $Fe_3O_4/TiO_2$ heterostructure (Fig. 4(f)) exhibited a significantly reduced Ms (1.658 emu $g^{-1}$), indicating substantial magnetic dilution and modification of exchange interactions upon Mn inclusion and $TiO_2$ coupling. Both materials had short hysteresis loops and low coercivity ($H_c$ = 32.56 Oe for FeMn/T-3), indicating soft ferromagnetic activity. The Mn-doped sample's significantly decreased remanence and squareness ratio ($M_r/M_s$ = 0.05) indicate near-superparamagnetic properties, allowing for easy magnetic recovery without residual agglomeration. Mn inclusion reduces magnetism relative to $Fe_3O_4/TiO_2$, yet the remaining magnetic response is sufficient for external magnetic separation, ensuring the photocatalyst's practical recyclability.[25]

The Scanning Electron Microscopy (SEM) was employed to analyze the morphologies and perform elemental analysis of the samples. The SEM analysis was conducted using a JEOL JSM-6510LA microscope. SEM images revealed morphologies characterized by fine aggregates clumping together, forming rounded shapes indicative of sintering during calcination.[26] The synthesized photocatalyst 0.75 FeMnT-3 displayed a spherical or rounded morphology due to the sintering of nanoparticles during calcination, as shown in Fig. 5(a–c). Energy Dispersive X-ray Spectroscopy (EDX) confirmed the dispersion of metals within the tri-composite Mn@$Fe_3O_4/TiO_2$ samples. The dominant peaks in the EDX spectra corresponded to titanium (Ti), oxygen (O), $Fe_3O_4$ and manganese (Mn). Fig. 5(d) illustrates the EDX analysis, validating the uniform dispersion of metals and supporting the integration of titanium with doped metallic impurities (Fe, Mn, and $TiO_2$).

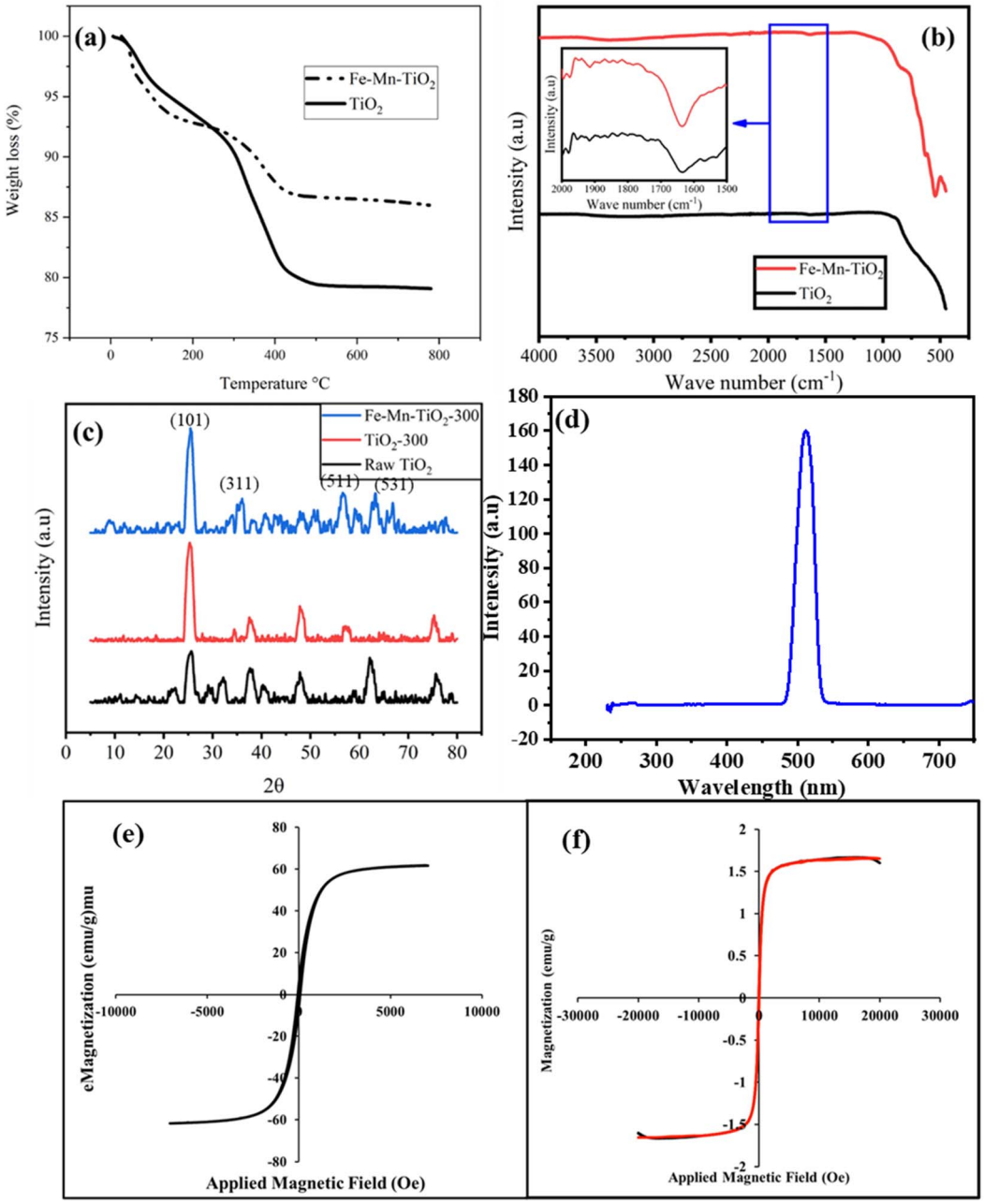


Fig. 4 Physicochemical analysis of the synthesized raw $TiO_2$, calcined $TiO_2$, and FeMnT (a) TGA (b) FTIR (c) XRD (d) PL, *M–H* curve using VSM analysis of (e) bare $Fe_3O_4$, and (f) FeMnT-3.

A detailed morphological analysis 0.75 FeMnT-3 revealed a well-defined core–shell structure using TEM analysis, as in Fig. 5(d1–d4). In the images, the darker spherical regions ($Fe_3O_4$ core) were encapsulated uniformly by lighter shells ($TiO_2$) with relatively uniform particle size distribution; spherical with slight agglomeration in shape were observed, possibly due to magnetic interactions and synthesis conditions (like pH, calcination temperature). However, well-defined and separated particles were also evident, suggesting efficient $TiO_2$ capping by dopant metal. High-resolution imaging showed a crystalline structure characterized by distinct lattice fringes, confirming the structural integrity of both $Fe_3O_4$ and titania. The tight but uniformly adhered titania shell specifies proficient charge transfer. At the same time, manganese (Mn) doping seems to affect both the lattice spacing and surface roughness, thereby enhancing the composite's photocatalytic potential.

SEM-EDS analysis (Fig. 5c1 and c2) reveals the presence of Fe, Ti, Mn, and O in the FeMnT photocatalyst, showing good Mn incorporation and integration of the $Fe_3O_4$ and $TiO_2$ components. The elemental composition of the Mn-FeT photocatalyst was examined verifies the presence of Fe, Ti, Mn, and O, indicating the creation of a $Fe_3O_4/TiO_2$ composite doped with Mn.

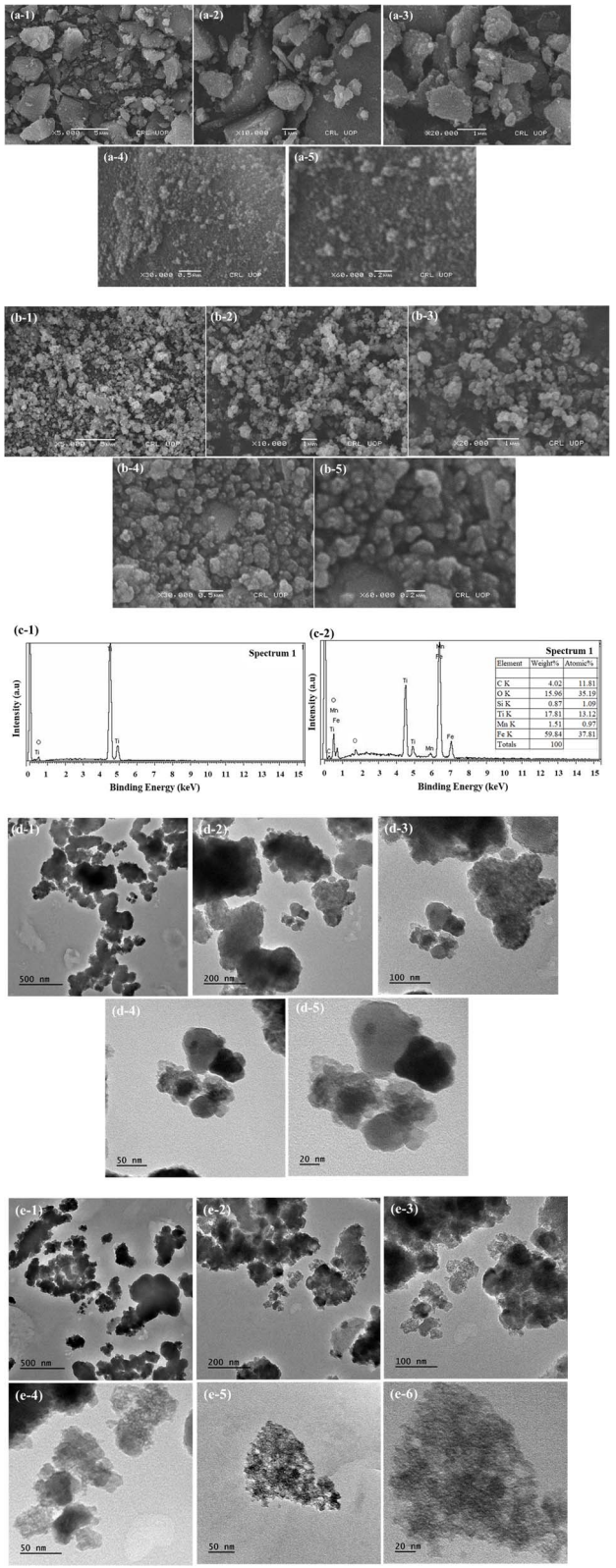


Fig. 5 SEM analysis of (a) bare $TiO_2$, (b) 0.75 FeMnT-3 at different resolutions, (c) SEM–EDS spectrum and quantitative elemental composition, and TEM analysis of (d) 0.75 FeMnT-3 and (e) 0.75 FeMnT-5, respectively, with varying magnifications.

Quantitative examination shows Fe as the dominating element (59.84 wt%, 37.81 at%), indicating a magnetic $Fe_3O_4$ core. Ti is present at 17.81 wt% (13.12 at%), confirming the $TiO_2$ component. Detectable Mn concentration (1.51 wt%, 0.97 at%) suggests that Mn incorporation was successful at modest loading levels. Oxygen is consistently detected (15.96 wt%), indicating metal oxide formation. Minor C and Si signals are caused by the carbon adhesive and silicon substrate utilized for SEM investigation. The combination of SEM-EDS, TEM morphology, XRD analysis, and magnetic measurements consistently supports the creation of a core–shell structured composite rather than a simple physical mixture.

### 3.6. Regeneration and recycling efficiency

After dye degradation and antibacterial experiments, FeMnT photocatalyst was recovered using an external magnet, thoroughly washed with ethanol and distilled water, and dried at 100 °C for two hours before reuse. Over five cycles, the photocatalyst exhibited good efficiency. A gradual decline in RY145 dye removal efficiency, decreasing from 89.45% (R1) to 69.30% (R5) (Fig. 6(a)). This reduction in performance might be attributed to photocatalyst deactivation, active site loss, and byproduct accumulation. Despite this decline, the photocatalyst maintained considerable activity, demonstrating its potential for reuse with further optimization.[27] For antibacterial activity, an initial 100% log reduction was observed for both *S. aureus* and *E. coli*. However, consecutive cycles showed declining bacterial inhibition, with *S. aureus* reducing to 92.47% (R2) and 68.03% (R5) (Fig. 6(b)) and *E. coli* declining to 78.87% (R2) and 61.39% (R5) (Fig. 6(b)). The cell wall differences between G+ive and G−ive bacteria influenced photocatalytic efficiency. The thicker peptidoglycan layer in *S. aureus* may lead to more organic byproduct release, which can adsorb onto the photocatalyst and hinder ROS generation. Similarly, *E. coli's* outer membrane (LPS layer) may enhance resistance to oxidative stress. The slight decrease in activity during cyclic tests (Fig. 6) is attributed to minor catalyst loss during recovery and surface fouling, not experimental error.

The primary causes of efficiency loss include surface contamination by organic residues and bacterial debris, photocatalyst leaching, structural modifications, reduced ROS production, and increased electron–hole recombination. Environmental factors such as pH and temperature may also contribute. While bacterial resistance is unlikely, these factors collectively impact long-term performance. To ensure sustainable and cost-effective use of FeMnT in photocatalytic disinfection and dye degradation, further stability enhancements and regeneration optimizations are necessary.[28–31]

### 3.7. Photocatalytic mechanism and mineralization of RY145

The photocatalytic degradation mechanism and mineralization were studied by active species trapping and COD analysis to investigate the role of various reactive species in RY145 photocatalytic degradation. Selective scavenger studies were conducted to identify the active species responsible for the breakdown of RY145 under visible light using FeMnT.

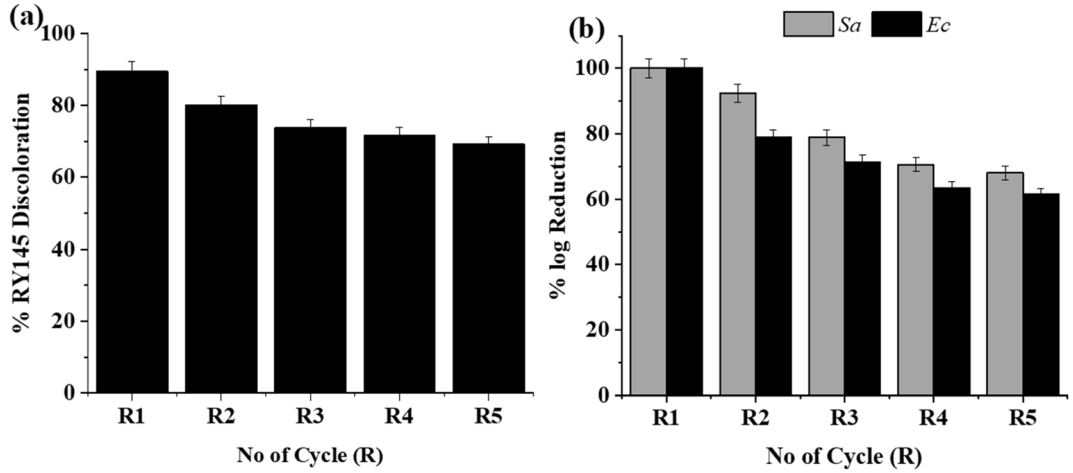


Fig. 6 Photocatalyst recycling studies using 0.75 FeMnT-3 against (a) RY145 photodegradation and (b) tested bacterial pathogens *S. aureus* and *E. coli*.

Isopropanol (IPA, 1 mM) was used to capture $^{\bullet}OH$ radicals, benzoquinone (BQ, 1 mM) for superoxide radicals ($O_2^{\bullet-}$), $AgNO_3$ (1 mM) for electrons, and $CaCl_2$ (1 mM) for holes ($h^+$). Ionic strength was controlled by $Na_2SO_4$ (1 mM). Fig. 7(a) and (b) showed that BQ inhibited degradation by 78.90%, confirming $O_2^{\bullet-}$ as the principal oxidative species, whereas IPA and $CaCl_2$ induced moderate-to-high inhibition (41.35% and 88.61%, respectively), showing secondary involvement of $^{\bullet}OH$ radicals and holes. $AgNO_3$ inhibited superoxide production by 92.41%, emphasizing the importance of conduction-band electrons. In accordance with efficient mineralization, the COD analysis of the treated solutions revealed a 67.2% decrease. Visible light stimulation moves electrons from the valence band to the conduction band of FeMnT, where CB electrons convert $O_2$ to $O_2^{\bullet-}$ and VB holes oxidize water/hydroxide to $^{\bullet}OH$. This process also contributes to dye oxidation. These findings clarify the role of scavenger and demonstrate the pseudo-first-order kinetics of RY145 degradation, which is primarily driven by superoxide radicals with contributions from holes and hydroxyl radicals.

The graph in Fig. 7(c) depicts the correlation between RY145 photodegradation and %COD elimination over time during photocatalysis. The effective breakdown of RY145 dye molecules is indicated by the dye degradation curve (open circles in Fig. 7(b)), which displays a sharp rise in photodegradation during the first 20 minutes and a plateau at about 89% after 60 minutes. The %COD removal pattern is similar, but lags slightly, with %COD removal approaching approximately 85% after 60 minutes. The lag indicates that the chromophoric groups of the dye are efficiently broken down, but the mineralization of organic intermediates into $CO_2$ and $H_2O$ takes more time.[13] The gap indicates the sequential process in which dye discoloration occurs before full organic load reduction in solution, confirming the photocatalyst's effectiveness in both dye degradation and partial mineralization. The time required for the complete mineralization was ~90 minutes under visible light irradiation. The close correlation between dye discoloration and mineralization (COD reduction) in the figure suggests that the photocatalytic process breaks down the chromophoric structure of the dye and effectively degrades the organic intermediates into smaller, less complex compounds, ultimately leading to mineralization ($CO_2$, $H_2O$, and inorganic ions). This strong alignment suggests a high degree of oxidative degradation rather than only partial dye fragmentation, which is frequent in advanced oxidation processes when reactive oxygen species (ROS) damage both the dye structure and its byproducts. This close trend is likely due to the catalyst's effectiveness in producing ROS while reducing the formation of persistent organic intermediates.

The FeMnT photocatalysts, due to the incorporation of Mn and $Fe_3O_4$ onto $TiO_2$, not only enhanced their reusability but also improved their antibacterial efficacy as evident by inactivating both G+ive and G−ive (*S. aureus* and *E. coli*) bacteria mainly through the generation of reactive oxygen species (ROS) following light exposure, triggering bacterial membranes and damaging DNA.[31] The photocatalytic mechanism was examined using scavengers to identify the specific roles of different reactive species, emphasizing the critical roles of $h^+$ and $H_2O_2$. The antibacterial approach may involve distinct mechanisms mainly by disrupting their outer membranes, cell structures, and cluster adsorption, leading to the malfunction of selective permeable barriers. Furthermore, the roles of $h^+$ and $H_2O_2$ reactive species are related to this antibacterial activity. Even after five cycles, FeMnT retained more than 90% of its bacterial elimination performance, according to recovery and reusability tests.[28–31] The combination of $Fe_3O_4/TiO_2$ produces effective antibacterial photocatalysts, promising applications in various fields like healthcare and environmental protection. Mn-incorporated $Fe_3O_4/TiO_2$ systems offer stable antibacterial effects without detachment or leaching concerns, providing an eco-friendly method to boost antibacterial activity while preserving photocatalytic performance.[32]

The $Fe_3O_4/TiO_2$ system's combined PL, VSM, and photocatalytic performance data demonstrate Mn's multifunctional

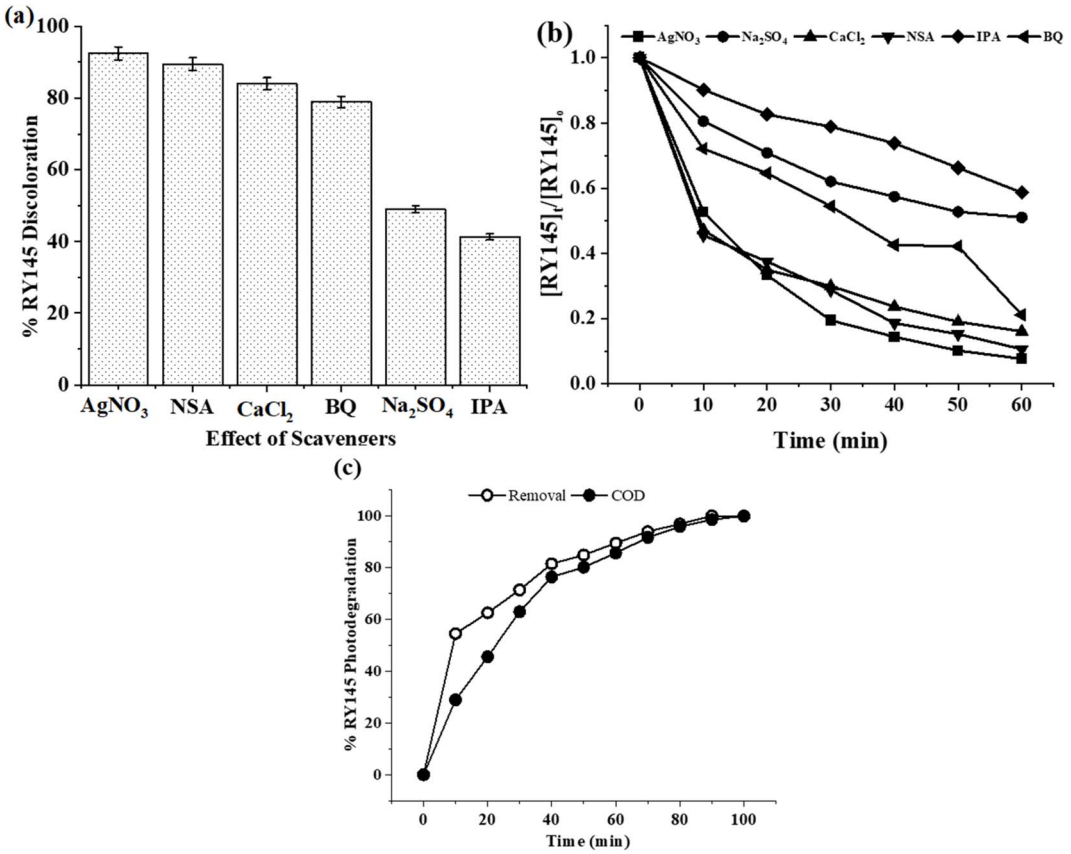


Fig. 7 (a) Active species trapping experiments showing the influence of specific scavengers on photocatalytic degradation performance, (b) Plot of $[RY145]_t/[RY145]_0$, (c) % discoloration *vs.* mineralization.

role. The improved 0.75 FeMnT-3 had much lower emission intensity in the visible range (~500–520 nm) compared to bare $TiO_2$, showing reduced radiative recombination and more efficient charge separation (PL study). This suppression demonstrates that Mn doping introduces regulated defect states and intermediate energy levels, allowing charge carrier trapping without producing an excessive number of recombination centers. The 0.75 FeMnT-3 preserves evident

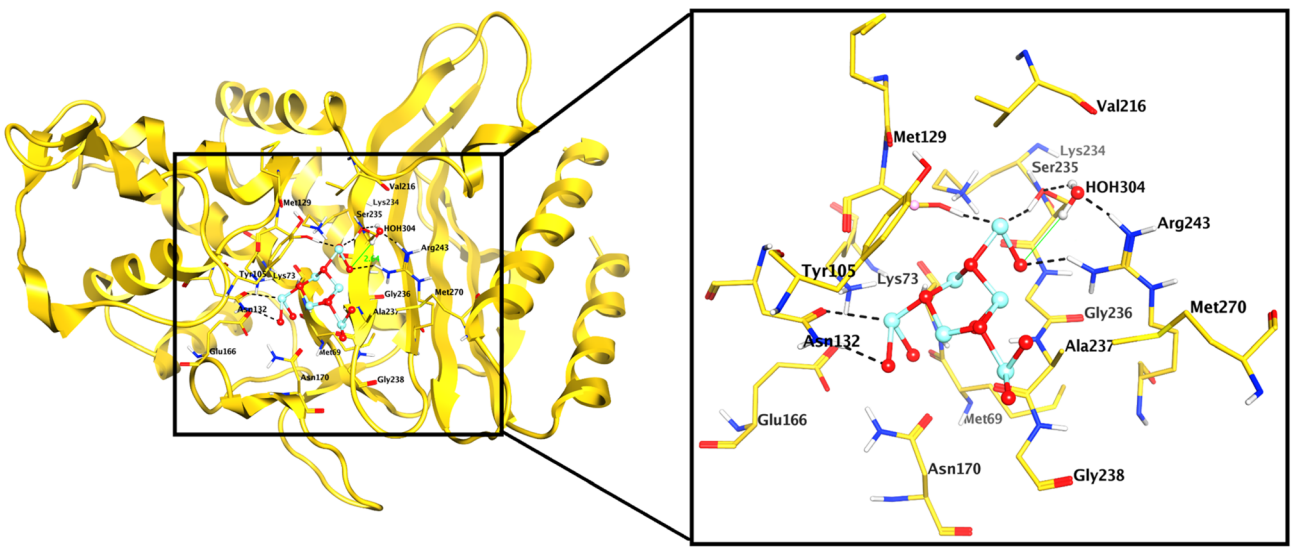


Fig. 8 The binding mode of the photocatalyst (represented by the cyan ball and sticks) is shown in the active site of β-lactamase enzyme (shown as yellow ribbons). The interactions with the active site residues are highlighted in the box, where bonds are depicted in black dashed lines, while solvent–ligand interaction is shown in green line.

ferromagnetic behavior with appropriate saturation magnetization for rapid magnetic recovery. This confirms that Mn incorporation does not undermine the magnetic functionality supplied by the $Fe_3O_4$ core. Mn-doped $TiO_2$ and the $Fe_3O_4$ core interact synergistically due to their retained magnetic sensitivity and increased interfacial charge transfer. As a result, the improved 0.75 FeMnT-3 photocatalyst achieves high photodegradation efficiency (89.5% within 60 min), revealing that Mn inclusion improves charge separation, magnetic recyclability, and overall photocatalytic performance.

### 3.8. Molecular docking

β-Lactamases are produced by several bacteria to disrupt the β-lactam ring of antibiotics, thereby inducing multiple bacterial antibiotic resistance and deactivating antibiotic properties. Since our photocatalyst showed excellent bactericidal activity, we docked nanoparticle into β-lactamase binding site, where the photocatalyst showed excellent interactions with multiple residues (Ser130, Asn132, Ser235, Arg243) and a nearby solvent molecule (HOH304). With these surface contacts, the photocatalyst exhibits a highly negative docking score ($-12.70$ kcal $mol^{-1}$), suggesting its good interactions. The Ti-linked oxygen atoms mediate hydrogen bonds with the side chains of Ser130 (2.83 Å), Ser235 (2.85 Å), Asn132 (2.85 Å), and Arg243 (3.08 Å). Additionally, a water molecule (HOH304) provides a hydrogen bond to one of these oxygen atoms at 3.22 Å. Moreover, one of the Ti atoms also mediates a metallic bond with the side chain of Asn132 at 2.83 Å, while Arg243 forms an ionic bond with one of the oxygen atoms (3.08 Å). These predicted binding of photocatalyst with β-lactamase, together with the highly negative docking score, suggest possible contact that may contribute secondarily to antibacterial effects. While its primary bactericidal activity is attributed to ROS-driven photocatalytic mechanisms, particularly relevant for β-lactam-resistant bacteria. The binding mode of photocatalyst is shown in Fig. 8.

## 4. Conclusion

Adding $Fe_3O_4$ photocatalysts significantly enhances the antibacterial activity of $TiO_2$ photocatalysts, showing potential for water treatment and disinfection applications. $Fe_3O_4/TiO_2$ and Mn@ $Fe_3O_4/TiO_2$ photocatalysts demonstrate potent antibacterial action under visible light, effectively deactivating both Gram-negative *(E. coli)* and Gram-positive *(S. aureus)* bacteria by targeting outer membranes and cell structures. The photocatalysts were prepared by a two-step method: Sol–Gel assisted wet impregnation with different $Fe_3O_4$ loading (0–1.5 wt%) and calcination temperature (300 and 500 °C). Screening experiments were conducted to identify the photocatalyst with maximum performance in terms of RY145% Removal. Photocatalysts with 0.75 $Fe_3O_4$ loading calcined at 300 °C showed the best performance by 89.57% RY-145 removal. Optimization was conducted by pH, photocatalyst dose, and dye concentration. Because of restricted light penetration, competing adsorption, and active site saturation, the removal efficacy decreases with increasing dye concentration, and the discoloration rate decreases because of the increased dye concentration. The presence of manganese as a dopant ion enhanced photocatalytic activity and could also increase the adsorption property, whereas recyclability and separation of the photocatalysts was assisted by the presence of a magnetic part that was iron oxide. The characterization revealed that the inclusion of Mn in $Fe_3O_4/TiO_2$ improved its structural, optical, and magnetic characteristics, allowing for effective RY145 photodegradation in visible light and easy recovery of the photocatalyst for sustainable reuse. Under visible light irradiation, the 0.75 FeMnT-3 particle calcined at 300 °C performed better at decolorizing RY-145. This might be due to (i) a narrowing of the band gap, effectively absorbing longer wavelength light, and the introduction of additional trapping locations, which might influence charge carrier durations, minimizing electron–hole recombination, thus leading to enhanced photocatalytic activity. The outstanding performance of Mn integrated $Fe_3O_4/TiO_2$ was recognized to high photo-generated electron–hole separation efficiency. Hydroxyl radicals ($^{\bullet}OH$) were identified as the main ROS species that play a significant role in the photocatalytic process. The significant alignment between discoloration and mineralization indicates the successful mineralization of dye molecules, emphasizing the catalyst's ability to break down and its intermediates. Molecular docking studies suggested that the photocatalyst's strong and stable binding to the β-lactamase active site, backed by many specific interactions and a very negative docking score, demonstrates its potential to disrupt resistance mechanisms and improve antibacterial efficacy.

## Author contributions

Sabahat Sabeen Butt, Shabnam Javaid: formal analysis, investigation and writing – original draft, Muhammad Saqib Khan and Rizwana Sarwar: supervision, writing – review and editing, software, analysis, validation, Sobia Ahsan Halim: software, writing – review and editing, Muhammad Bilal: writing – review and editing; Ajmal Khan, Ahmed Al-Harrasi, Khayala Mammadova and S. Tasqeeruddin: writing – review and editing, funding acquisition, validation, Nadia Riaz: supervision, conceptualization, resources, funding acquisition, methodology, writing – review and editing.

## Conflicts of interest

The authors declare no conflicts of interest.

## Data availability

The data supporting this article have been included as part of the supplementary information (SI). Supplementary information is available. See DOI: https://doi.org/10.1039/d6ra00672h.

## Acknowledgements

The authors extend their appreciation to the Deanship of Research and Graduate Studies at King Khalid University, KSA, for funding this work through Small Research Group under grant number RGP.1/73/46.

## References

1 K. Kodam, I. Soojhawon, P. Lokhande and K. Gawai, *World J. Microbiol. Biotechnol.*, 2005, **21**, 367–370.
2 R. Saini and K. Choudhary, in *Hazardous Chemicals*, Elsevier, 2025, pp. 469–481.
3 Z. Momeni, F. Modalaliyan, A. Fatehizadeh, S. Ghanbari, A. Ebrahimi, M. Khiadani, E. Taheri and M. Rezakazemi, *Environ. Res.*, 2024, **255**, 119111.
4 A. Vickram, S. I. Shofia, J. Palanivelu, S. Karishma, A. Saravanan and P. Yaashikaa, *Groundw. Sustain. Dev.*, 2024, 101315.
5 K. Ramamurthy, P. S. Priya, R. Murugan and J. Arockiaraj, *Environ. Sci. Pollut. Res.*, 2024, **31**, 33190–33211.
6 S. Dutta, S. Adhikary, S. Bhattacharya, D. Roy, S. Chatterjee, A. Chakraborty, D. Banerjee, A. Ganguly, S. Nanda and P. Rajak, *J. Environ. Manage.*, 2024, **353**, 120103.
7 T. N Lotha, V. Sorhie, P. Bharali and L. Jamir, *ChemistrySelect*, 2024, **9**, e202304093.
8 M. S. Khan, N. Riaz, S. Rehman, L. Chenhui, A. J. Shaikh, M. Arfan, I. Zeb, M. Arshad, F. Hafeez and M. Bilal, *Environ. Sci. Pollut. Res.*, 2023, **30**, 124992–125005.
9 Y. Song, C. Shang, P. Westerhoff and L. Ling, *Water Res.*, 2024, **257**, 121682.
10 X. Tian, X. Cai, Z. Zeng, Y. He, X. Xu, L. Lei, C. Xu, X. Xu, Y. Xu and P. Li, *Chem. Eng. J.*, 2024, **498**, 155304.
11 B. Jiang, M. Mu, Y. Zhou, J. Zhang and W. Li, *Small*, 2024, 2311897.
12 E. E. A. Suarez, M. E. R. Jalil, M. A. F. Baldo and S. A. Cuozzo, *Environ. Sci.: Nano*, 2025, **12**, 979–1011.
13 S. N. Ul Ain, M. S. Khan, N. Riaz, A. Khan, A. Sarwar, A. Khalid, A. Jan, Q. Mahmood and A. Al-Harrasi, *ACS Omega*, 2024, **9**, 13803–13817.
14 M. S. Khan, J. A. Shah, N. Riaz, T. A. Butt, A. J. Khan, W. Khalifa, H. H. Gasmi, E. R. Latifee, M. Arshad, A. A. A. Al-Naghi, A. Ul-Hamid, M. Arshad and M. Bilal, *Nanomaterials*, 2021, **11**, 436.
15 S. K. Fatima, A. S. Ceesay, M. S. Khan, R. Sarwar, M. Bilal, J. Uddin, A. Ul-Hamid, A. Khan, N. Riaz and A. Al-Harrasi, *ACS Omega*, 2023, **8**(3), 3007–3016.
16 B. Guan, J. Chen, Z. Zhuang, L. Zhu, Z. Ma, X. Hu, C. Zhu, S. Zhao, K. Shu, H. Dang, T. Zhu and Z. Huang, *Catal. Lett.*, 2024, **155**, 5.
17 Y. Pajouhan, S. Sabbaghi, K. Rasouli, J. Rasouli, W. Dastyar and E. Andiroglu, *Process Saf. Environ. Prot.*, 2024, **190**, 1149–1163.
18 G. Ebrahimzadeh-Rajaei, *Theor. Found. Chem. Eng.*, 2022, **56**, 1088–1099.
19 A. Zane, R. Zuo, F. A. Villamena, A. Rockenbauer, A. M. Digeorge Foushee, K. Flores, P. K. Dutta and A. Nagy, *Int. J. Nanomed.*, 2016, 6459–6470.
20 C. Xu, J. Zheng and A. Wu, in *$TiO_2$ Nanoparticles*, 2020, pp. 105–132, DOI: 10.1002/9783527825431.ch3.
21 S. Ma, S. Zhan, Y. Jia and Q. Zhou, *ACS Appl. Mater. Interfaces*, 2015, **7**, 21875–21883.
22 S. Preda, J. Pandele-Cuşu, S. V. Petrescu, E. M. Ciobanu, G. Petcu, D. C. Culiă, N. G. Apostol, R. M. Costescu, I. Raut, M. Constantin and L. Predoană, *Gels*, 2022, **8**, 673.
23 J. Rawat, A. Rawat, H. Sharma and C. Dwivedi, *ACS Appl. Energy Mater.*, 2024, **7**, 6071–6083.
24 A. Valadi Palliyalil, A. V. Thelappurath, D. Wojtas, N. Pizúrová, M. Pávková Goldbergová and S. G. Ullattil, *ACS Appl. Mater. Interfaces*, 2026, **18**(6), 10476–10490.
25 V. Maria Vinosel, M. Asisi Janifer, S. Anand and S. Pauline, *Int. J. Mech. Eng. Mater. Sci.*, 2017, **9**, 1–7.
26 A. Albeladi, Z. Khan, S. A. Al-Thabaiti, R. Patel, M. A. Malik and S. Mehta, *Catalysts*, 2024, **14**, 71.
27 V. Gupta and S. Singh, *Chem. Inorg. Mater.*, 2024, **3**, 100051.
28 M. Abbas, B. P. Rao, V. Reddy and C. Kim, *Ceram. Int.*, 2014, **40**, 11177–11186.
29 H. Baniamerian, M. Safavi, M. Alvarado-Morales, P. Tsapekos, I. Angelidaki and S. Shokrollahzadeh, *Environ. Res.*, 2018, **166**, 497–506.
30 T. Xin, M. Ma, H. Zhang, J. Gu, S. Wang, M. Liu and Q. Zhang, *Appl. Surf. Sci.*, 2014, **288**, 51–59.
31 K. Tedsree, N. Temnuch, N. Sriplai and S. Pinitsoontorn, *Mater. Today: Proc.*, 2017, **4**, 6576–6584.
32 E. A. Elgohary, Y. M. A. Mohamed, H. A. El Nazer, O. Baaloudj, M. S. S. Alyami, A. El Jery, A. A. Assadi and A. Amrane, *Catalysts*, 2021, **11**, 1498.